Article

Earth's ambipolar electrostatic field and its role in ion escape to space

Glyn A. Collinson[1,2,3✉], Alex Glocer[1], Robert Pfaff[1], Aroh Barjatya[4], Rachel Conway[4], Aaron Breneman[1], James Clemmons[5], Francis Eparvier[6], Robert Michell[1], David Mitchell[7], Suzie Imber[8], Hassanali Akbari[1,2], Lance Davis[4], Andrew Kavanagh[9], Ellen Robertson[1], Diana Swanson[5], Shaosui Xu[7], Jacob Miller[1,10], Timothy Cameron[1], Dennis Chornay[1], Paulo Uribe[1], Long Nguyen[1], Robert Clayton[4], Nathan Graves[4], Shantanab Debchoudhury[4], Henry Valentine[4], Ahmed Ghalib[11] & The Endurance Mission Team*

Cold plasma of ionospheric origin has recently been found to be a much larger contributor to the magnetosphere of Earth than expected[1–3]. Numerous competing mechanisms have been postulated to drive ion escape to space, including heating and acceleration by wave–particle interactions[4] and a global electrostatic field between the ionosphere and space (called the ambipolar or polarization field)[5,6]. Observations of heated O^+ ions in the magnetosphere are consistent with resonant wave–particle interactions[7]. By contrast, observations of cold supersonic H^+ flowing out of the polar ionosphere[8,9] (called the polar wind) suggest the presence of an electrostatic field. Here we report the existence of a $+0.55 \pm 0.09$ V electric potential drop between 250 km and 768 km from a planetary electrostatic field ($E_\parallel\oplus = 1.09 \pm 0.17\ \mu V\ m^{-1}$) generated exclusively by the outward pressure of ionospheric electrons. We experimentally demonstrate that the ambipolar field of Earth controls the structure of the polar ionosphere, boosting the scale height by 271%. We infer that this increases the supply of cold O^+ ions to the magnetosphere by more than 3,800%, in which other mechanisms such as wave–particle interactions can heat and further accelerate them to escape velocity. The electrostatic field of Earth is strong enough by itself to drive the polar wind[9,10] and is probably the origin of the cold H^+ ion population[1] that dominates much of the magnetosphere[2,3].

There is substantial ambiguity in the strength of the electrostatic field of Earth, its physical drivers, and its role in the escape of ions to space. At a minimum, this field is thought to be underpinned by an ambipolar electric field[8,9]. These fields are generated as ionospheric electrons attempt to escape to space under their own thermal pressure. As the electrons attempt to pull away from the heavier ions, an ambipolar field arises to maintain charge neutrality[6,11]. However, ambipolar fields have not been unambiguously measured in nature because of their weak strength. If the ambipolar field is the only mechanism driving the electrostatic field of Earth, then the resulting electric potential drop across the exobase transition region (200–780 km) could be as low as about 0.4 V (ref. 12). However, modelling studies have proposed that the ambipolar field of Earth may be enhanced to several volts by suprathermal (>1 eV) photoelectrons that are omnipresent above the sunlit hemisphere of Earth[12]. Furthermore, recent observations at Venus and Mars have shown that other physical processes can strongly enhance the electric potential of a terrestrial planet by as much as tens of volts[6,13–16]. The few previous attempts to measure the electrostatic field of Earth have been able to

establish only an upper bound on the electric potential drop in the ionosphere of ≤2 V (refs. 17,18). If it is as strong as 2 V, then it would be directly responsible for around 20% of the escape of O^+ ions to space. Even a small difference of ±0.2 V relative to a low-end case of a 0.4 V potential would make a substantial difference to the fraction of H^+ directly escaping from Earth by this mechanism (approximately 50%, 0.2 V compared with 100%, 0.6 V) (ref. 19).

The NASA *Endurance* rocket mission[19] (yard number 47.001) launched from Ny-Ålesund, Svalbard, on 11 May 2022 at 01:31:00 Greenwich Mean Time (GMT) (Fig. 1d) to an altitude of 768 km (Fig. 1a,c) to attempt to make the first successful measurement of the intrinsic electrostatic field of Earth. The high-latitude launch site (78.93° N) was selected to fly on open magnetic field lines above the polar caps (Fig. 1b) that provide a key pathway for ion outflow to the magnetosphere. The launch occurred during geomagnetically quiet conditions (Extended Data Fig. 7) to have as few perturbations in the environment as possible during the observations. The trajectory was designed so that one would not expect a measurable difference in the electrostatic field along the
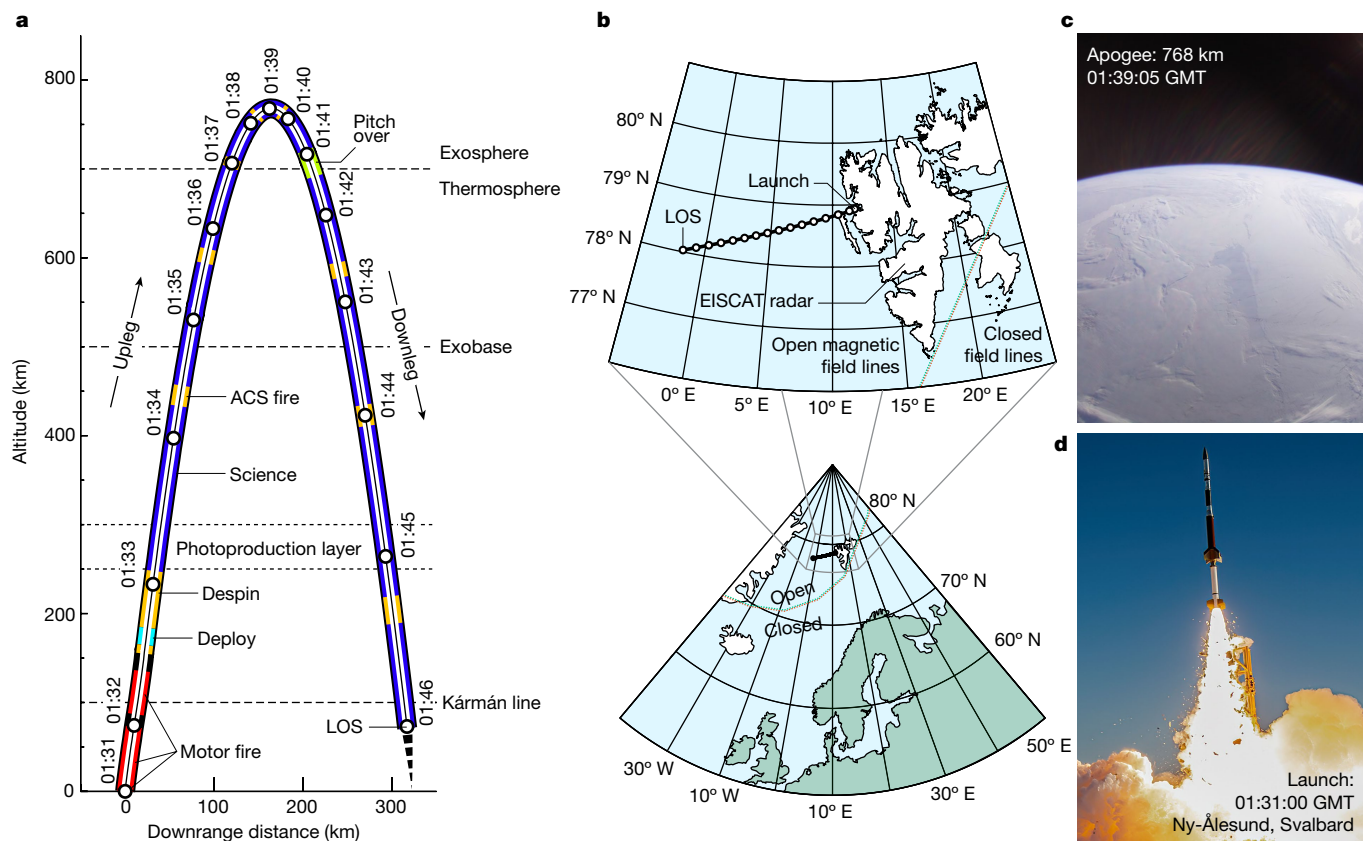
Fig. 1 | The flight of the NASA rocketship *Endurance*. a, Scale map of the parabolic trajectory of the spacecraft colour coded by mission phase, showing regions explored of the upper polar atmosphere and ionosphere. Circles mark 1-min intervals beginning at launch at 01:31 GMT. The region marked 'Photoproduction layer' refers to the peak of He-II photoelectron production. **b**, Map of ground track of the flight from launch to LOS with respect to the open and closed magnetic field line boundary of the magnetic dipole field of Earth and the location of the EISCAT Svalbard radar that made simultaneous measurements of the ionosphere. **c**, Photograph taken by the Panoramic Camera near apogee showing the sunlit geographic North Pole of Earth. Image credit: NASA. **d**, Photograph showing booster ignition and lift-off of the *Endurance*. Image credit: Leif Jonny Eilertsen/Andøya Space.

trajectory. Furthermore, we would not expect any temporal changes during the approximately 13-min duration of science collection.

The scientific instruments were successfully deployed (Fig. 1a, teal) near 150 km altitude on the upleg, just 9.5 s after jettison of the third-stage booster motor. *Endurance* was then de-spun and aligned within 1° of the ambient magnetic field using cold-gas Attitude Control System (ACS) thrusters. Science operations began at $T + 125$ s after the launch at an altitude of 248 km on the upleg. The mission alternated between 70 s of uncontaminated science collection at which the ACS was off (Fig. 1a, blue), followed by 10 s at which the ACS re-aligned the spacecraft with the ambient magnetic field (Fig. 1a, amber). Apogee (768.03 km) (Fig. 1c) was chosen to measure the electric potential across the exobase (around 500 km), above which ions stop being collisionally bound to the neutral atmosphere and are free to escape upwards. *Endurance* gathered continuous data until loss of signal (LOS) at $T + 900.6$ s at an altitude of 70.94 km during re-entry into the atmosphere. The wreckage impacted the Greenland Sea near 78°1′40.31″ N, 1°41′55.8″ W, coming to rest in approximately 2,900 m of water.

The total potential drop below the *Endurance* was measured from the shift in the energy of electrons outflowing from the ionosphere[13,14,17,18]. The intense He-II emission line of the Sun at 30.4 nm is a source of photoionization throughout our solar system (ref. 20). This mono-energetic radiation generates several discrete peaks (photopeaks) in the energy spectrum of electrons originating in the dayside ionosphere. Figure 2 shows the in situ measurements of these He-II photopeaks by the photoelectron spectrometer (PES), a technology developed for the mission[21]. The brightest He-II photopeak observed by PES was dominated by the N_2 $A^2\Pi_u$ atomic transition, which generates electrons at 24.09 eV (refs. 22,23). He-II photopeaks are generated only over a narrow altitude range (250–300 km during the flight). Above this photoproduction region, the PES observed a decrease in the energy of the photopeak with increasing altitude (Fig. 2c (red line) and Extended Data Fig. 2). This is consistent with the presence of a weak positive electrical potential across the exobase of Earth, which slows electrons as they attempt to escape to space (but will push the ions outwards). The farther the *Endurance* drifted from Earth, the greater the electric potential drop below, resulting in a progressively larger shift of the photopeak towards lower energies (Fig. 2c and Extended Data Fig. 3).

Figure 3a,b shows the ionospheric electric potential drop of Earth measured from this photopeak energy shift. These data have been corrected for the electrical potential of the spacecraft[13] from the Swept Langmuir Probe (SLP)[19] (Extended Data Fig. 4e), with a supporting cross-check by the Electromagnetic Fields and Waves (FIELDS) instrument[19] (Extended Data Fig. 5b). Both SLP and FIELDS instruments gave a consistent measurement of spacecraft potential over the flight, albeit with closer agreement on the upleg.

Endurance measured two near-vertical profiles of electric potential versus altitude, first on the upleg (250 km to apogee) and again on the downleg (apogee to LOS). A mean potential drop of 0.55 ± 0.09 V was measured across the exobase of Earth (250–768 km). By taking the average gradient of these near-simultaneous vertical measurements, we find that the ionosphere of Earth intrinsically generates an electrical field parallel to its magnetic field ($E_\parallel$) of 1.09 ± 0.17 μV m^{-1}.
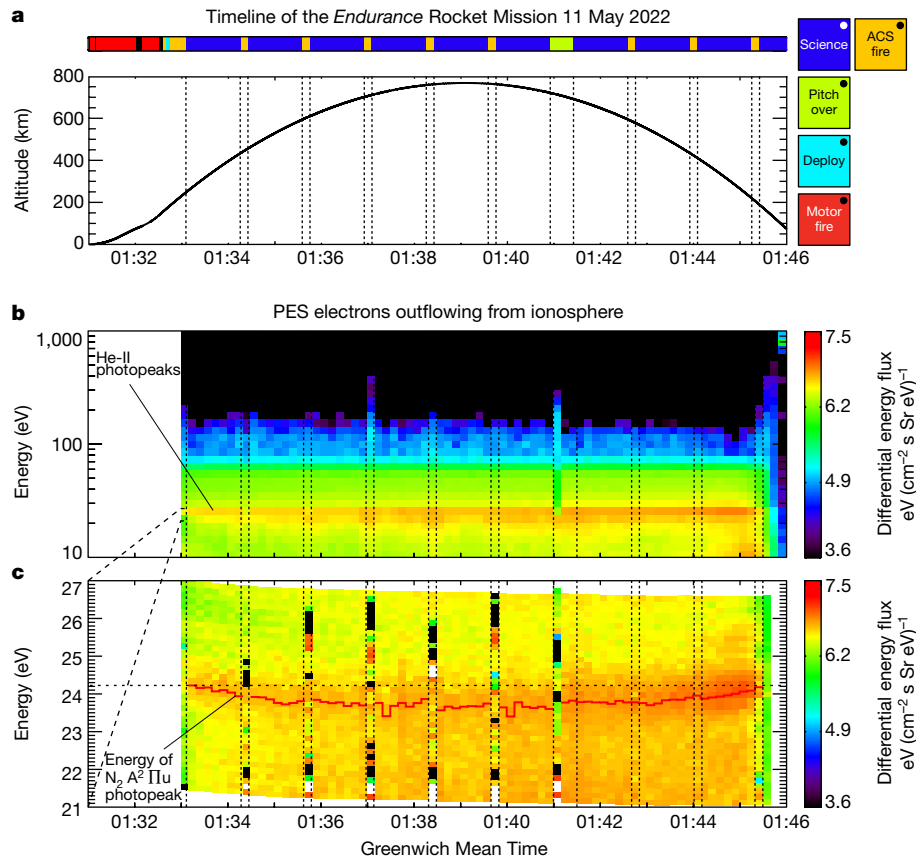
Fig. 2 | Measurements of the energy spectra of electrons escaping from ionosphere of Earth by the PES. a, Colour-coded timeline (consistent with Fig. 1a) of the mission and altitude of the rocketship during the flight. Vertical dashed lines on all three panels denote science collection periods. **b**, Standard resolution (15% $\Delta E/E$) time versus energy spectrogram of the differential energy flux of electrons outflowing from the ionosphere of Earth. **c**, High-resolution (0.5% $\Delta E/E$) time versus energy spectrogram resolving the He-II photopeaks and their shift to lower energies with altitude resulting from the electrostatic field of Earth. The peak energy of the primary He-II photopeak is overplotted in red. These data have been corrected for the absolute spacecraft potential[19] using measurements by the SLP instrument.

Using SLP measurements of electron density (n_e) and temperature (t_e), we can calculate the electron thermal pressure ($P_e = n_e k_b T_e$). By taking the vertical gradient of electron pressure (∇P_e), we can compare the parallel electric field ($E_\parallel$) against what would be expected from a pure ambipolar field. The derivation of the ambipolar field has been presented in numerous previous publications (also in the Methods) and is found by solving for $E_\parallel$ in the steady-state electron momentum equation[11,24,25]. To the first order, $E_\parallel \approx -\nabla P_e/qn_e$ (refs. 26–28). We find a close agreement between this prediction (Fig. 3a,b, orange region) and our observations (Fig. 3a,b, diamonds). Thus, we conclude the only source of electrical potential was a classical electron pressure-driven ambipolar field. Unlike at Venus[13,15,16] and Mars[14,29], we find no evidence for additional mechanisms contributing to the electrostatic field of Earth.

Using classical ambipolar diffusion theory[30], we calculate two altitude profiles of predicted plasma density during the flight of *Endurance*. The first without the contribution of $E_\parallel$ (Fig. 3c,d, red dashed line) and the second with the measured 1.09 µV m^{-1} field (Fig. 3c,d, solid blue line). The latter (Fig. 3c,d, solid blue line) matches closely with the density profile from (1) in situ measurement by the SLP instrument (orange region), (2) simultaneous remote sensing by EISCAT radar (green region) (Extended Data Fig. 6) and is in good agreement with (3) the prediction by the International Reference Ionosphere (IRI) model (black dotted line). This close agreement gives an additional cross-check on the interpretation of the photoelectron peak shift as resulting from an ambipolar electric field.

The measurement of the electrostatic field of Earth has important consequences for our understanding of the structure of the topside ionosphere of Earth and the supply of heavy O$^+$ ions into the magnetosphere. No further physical mechanisms were required to explain the observations of plasma density versus altitude (Fig. 3c,d). This implies that the ambipolar field was the primary driver of the structure of the topside polar ionosphere during the quiet geomagnetic conditions chosen for the flight. This analysis is specific to the near-vertical magnetic field lines near the magnetic poles, and at lower latitudes additional transport processes should be accounted for[30].

Comparing the two altitude profiles, with and without the effect of $E_\parallel$, enables us to quantify the impact of the ambipolar field on the vertical transport of O$^+$ ions in the polar cap. The field increases the scale height of the ionosphere by 271% (from $H = 77.0$ km to $H = 208.9$ km). This enhances plasma density near the boundary of the magnetosphere (that is, near apogee at 768 km) by more than 3,800%. This demonstrates experimentally that the ambipolar field provides the initial lift to higher altitudes for heavy ions in the polar caps at which other acceleration mechanisms such as wave–particle interactions can come into play to drive them to escape velocity[4,7].

The measurements support the hypothesis that the ambipolar electric field is the primary driver of ionospheric H$^+$ outflow, and of the supersonic polar wind of light ions escaping from the polar caps. The 1.09 µV m^{-1} field measured over the sunlit polar region is sufficient to provide an outward force on ionospheric H$^+$ of 10.6 times that of gravity. This value is close to eight times the gravity expected from theoretical calculations assuming an isothermal O$^+$-dominated ionosphere with an electric field driven purely by the electron pressure gradient[30]. The escape velocity at the apogee of *Endurance* (768 km) is
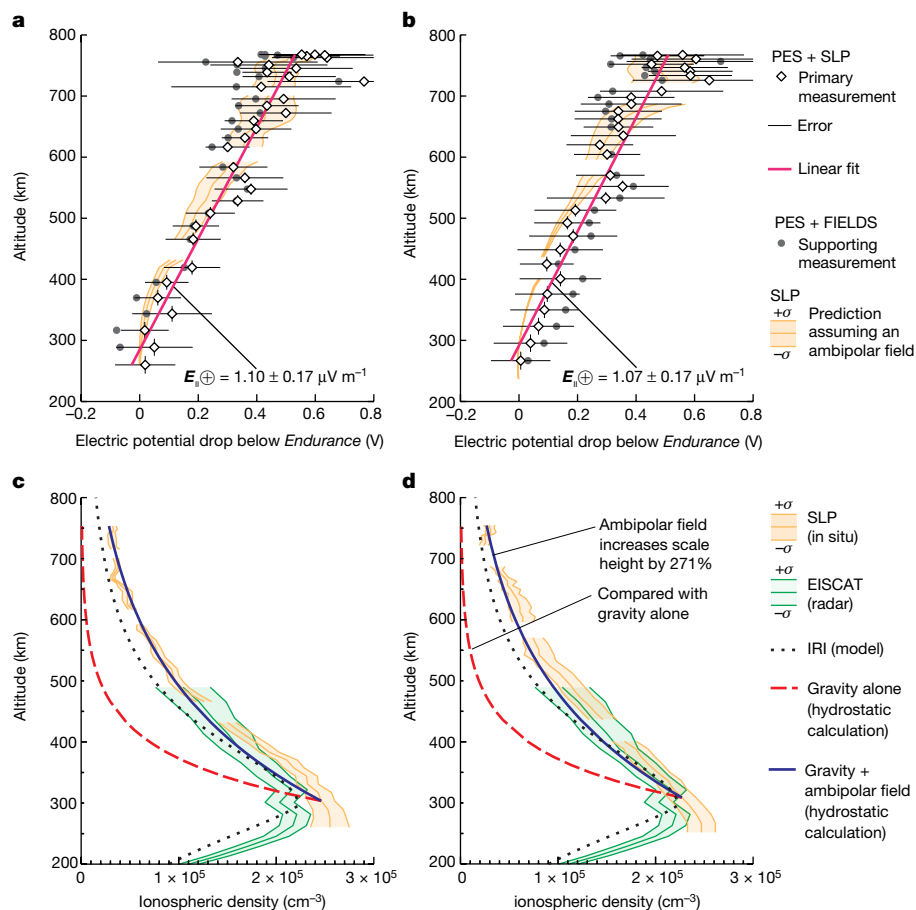
Fig. 3 | The electrical potential drop of Earth across the exobase and its role in controlling the structure of the topside polar ionosphere. a,b, Upleg (**a**) and downleg (**b**) measurements of the electric potential drop of Earth. White diamonds show the relative shift in the He-II photopeaks when corrected for the spacecraft potential measured by the SLP instrument, with a linear fit in pink. Error bars are described in the Methods. The grey dots show a correction for spacecraft potential by the FIELDS instrument for cross-checking with SLP. The orange region shows the parallel potential drop that would be expected from a classical ambipolar field driven by the electron pressure gradient as measured by SLP. **c,d,** Upleg (**c**) and downleg (**d**) measurements of the structure of the topside polar ionosphere of Earth measured in situ by SLP (orange region) and remotely by EISCAT radar (green region). The black dotted lines show a prediction by the IRI empirical model. Dashed red lines show how the ionosphere of Earth should fall off according to a classical hydrostatic equilibrium in which gravity is the only controlling force. The dark blue lines show hydrostatic equilibrium at which the intrinsic planetary electric field measured near Earth by *Endurance* partially counters gravity.

10.62 km s^{-1}, corresponding to an escape energy for H$^+$ of 0.58 eV. This escape energy is identical within the errors to the total potential drop measured between 250 km and 767 km of 0.55 ± 0.09 V. Therefore, H$^+$ accelerated by this field will not fall back to the atmosphere. Moreover, this field accelerates plasmas without heating. Thus, we posit that the ambipolar field is the most likely outflow mechanism for the dense cold plasmas persistently observed throughout the magnetosphere[1,2].

Online content

Any methods, additional references, Nature Portfolio reporting summaries, source data, extended data, supplementary information, acknowledgements, peer review information; details of author contributions and competing interests; and statements of data and code availability are available at https://doi.org/10.1038/s41586-024-07480-3.

1. Engwall, E. et al. Earth's ionospheric outflow dominated by hidden cold plasma. *Nat. Geosci.* **2**, 24–27 (2009).
2. Haaland, S. et al. Estimating the capture and loss of cold plasma from ionospheric outflow. *J. Geophys. Res. Space Phys.* **117**, A07311 (2012).
3. André, M., Toledo-Redondo, S. & Yau, A. W. in *Space Physics and Aeronomy Collection Vol. 2: Magnetospheres in the Solar System* (eds Maggiolo, R. et al.) Geophysical Monograph 259 (American Geophysical Union, Wiley, 2021).
4. Kistler, L. M. et al. Cusp and nightside auroral sources of O+ in the plasma sheet. *J. Geophys. Res. Space Phys.* **124**, 10036–10047 (2019).
5. Strangeway, R. J., Ergun, R. E., Su, Y.-J., Carlson, C. W. & Elphic, R. C. Factors controlling ionospheric outflows as observed at intermediate altitudes. *J. Geophys. Res. Space Phys.* **110**, A03221 (2005).
6. Collinson, G. et al. Ionospheric ambipolar electric fields of Mars and Venus: comparisons between theoretical predictions and direct observations of the electric potential drop. *Geophys. Res. Lett.* **46**, 1168–1176 (2019).
7. Moore, T. E. & Khazanov, G. V. Mechanisms of ionospheric mass escape. *J. Geophys. Res. Space Phys.* **115**, A00J13 (2010).
8. Axford, W. I. The polar wind and the terrestrial helium budget. *J. Geophys. Res.* **73**, 6855–6859 (1968).
9. Banks, P. M. & Holzer, T. E. The Polar Wind. *J. Geophys. Res. Space Phys.* **73**, 6846–6854 (1968).
10. Li, K. et al. The effects of the polar rain on the polar wind ion outflow from the nightside ionosphere. *J. Geophys. Res. Space Phys.* **128**, e2023JA031496 (2023).
11. Varney, R. H., Solomon, S. C. & Nicolls, M. J. Heating of the sunlit polar cap ionosphere by reflected photoelectrons. *J. Geophys. Res. Space Phys.* **119**, 8660–8684 (2014).
12. Khazanov, G. V., Liemohn, M. W. & Moore, T. E. Photoelectron effects on the self-consistent potential in the collisionless polar wind. *J. Geophys. Res. Space Phys.* **102**, 7509–7521 (1997).
13. Collinson, G. A. et al. The electric wind of Venus: a global and persistent "polar wind"-like ambipolar electric field sufficient for the direct escape of heavy ionospheric ions. *Geophys. Res. Lett.* **43**, 5926–5934 (2016).
14. Xu, S. et al. Field-aligned potentials at Mars from MAVEN observations. *Geophys. Res. Lett.* **45**, 10,119–10,127 (2018).
15. Xu, S., Frahm, R. A., Ma, Y., Luhmann, J. G. & Mitchell, D. L. Magnetic topology at Venus: new insights into the Venus plasma environment. *Geophys. Res. Lett.* **48**, e2021GL095545 (2021).

16. Collinson, G. A. et al. A survey of strong electric potential drops in the ionosphere of Venus. *Geophys. Res. Lett.* **50**, e2023GL104989 (2023).

17. Coates, A. J., Jonstone, A. D., Sojka, J. J. & Wrenn, G. L. Ionospheric photoelectrons observed in the magnetosphere at distances up to 7 earth radii. *Planet. Space Sci.* **33**, 1267–1275 (1985).

18. Fung, S. F. & Hoffman, R. A. A search for parallel electric fields by observing secondary electrons and photoelectrons in the low-altitude auroral zone. *J. Geophys. Res. Space Phys.* **96**, 3533–3548 (1991).

19. Collinson, G. et al. The *Endurance* Rocket Mission. *Space Sci. Rev.* **218**, 39 (2022).

20. Coates, A. J. et al. Ionospheric photoelectrons: comparing Venus, Earth, Mars and Titan. *Planet. Space Sci.* **59**, 1019–1027 (2011).

21. Collinson, G. A. et al. Rocket measurements of electron energy spectra from Earth's photoelectron production layer. *Geophys. Res. Lett.* **49**, e2022GL098209 (2022).

22. Gardner, J. L. & Samson, J. A. R. 304 Å photoelectron spectra of CO, N_2, O_2 and CO_2. *J. Electron Spectros. Relat. Phenomena* **2**, 259–266 (1973).

23. Goembel, L., Doering, J. P., Morrison, D. & Paxton, L. J. Atmospheric O/N_2 ratios from photoelectron spectra. *J. Geophys. Res.* **102**, 7411–7419 (1997).

24. Gombosi, T. I. & Nagy, A. Time-dependent modeling of field-aligned current-generated ion transients in the polar wind. *J. Geophys. Res.* **94**, 359–369 (1989).

25. Liemohn, M. W., Khazanov, G. V., Moore, T. E. & Guiter, S. M. Self-consistent superthermal electron effects on plasmaspheric refilling. *J. Geophys. Res.* **102**, 7523–7536 (1997).

26. Godbole, N. H. et al. Observations of ion upflow and 630.0 nm emission during pulsating aurora. *Front. Phys.* **10**, 997229 (2022).

27. Wahlund, J.-E., Opgenoorth, H. J., Häggström, I., Winser, K. J. & Jones, G. O. L. EISCAT observations of topside ionospheric ion outflows during auroral activity: revisited. *J. Geophys. Res.* **97**, 3019–3037 (1992).

28. Wu, J. et al. Observations of the structure and vertical transport of the polar upper ionosphere with the EISCAT VHF radar. II - first investigations of the topside O(+) and H(+) vertical ion flows. *Ann. Geophys.* **10**, 375–393 (1992).

29. Collinson, G. et al. Electric Mars: a large trans-terminator electric potential drop on closed magnetic field lines above Utopia Planitia. *J. Geophys. Res. Space Phys.* **112**, 2260–2271 (2017).

30. Schunk, R. & Nagy, A. *Ionospheres* (Cambridge Univ. Press, 2009).

The Endurance Mission Team

S. Adkins[1], H. Akbari[1,2], R. Albano[2], L. Baddeley[12], H. Bahr[13], G. Bain[11], C. Bancroft[5], A. Barjatya[4], A. Barrie[1], M. Binder[11], S. Bissett[11], K. Blix[13], A. Bolton[5], B. Bonsteel[11], H. Borgen[13], D. Bowden[11], D. Bowker[11], E. Bowlen[2], M. Bradshaw[11], A. Breneman[1], G. Bridges[11], T. Cameron[1], M. Campbell[11], P. Cathell[11], D. Chornay[1], R. Clayton[4], J. Clemmons[5], G. Collinson[1,2,3], L. Conser[11], R. Conway[4], L. Davis[4], S. Debchoudhury[4], P. Demaine[5], D. Detwiler[11], M. Disbrow[11], J. Doughty[11], L. Eilertsen[13], S. Ellis[5], F. Eparvier[6], R. Ethridge[11], R. Fahringer[11], J. Farrell[11], M. Francheshini[5], C. Frost[5], T. Gass[11], A. Ghalib[11], A. Glocer[1], C. Grabusky[11], N. Graves[4], I. Haggstrom[14], P. Hanssen[13], G. Harlan[11], T. Harper[11], H. Haugh[11], E. Helgesen[14], J. Henderson[11], D. Henderson[11], K. Herseth[13], S. Imber[8], K. Jensen[13], T. Jester[11], R. Jillard[11], E. Johnson[11], H. Johnson[11], G. Jones[11], T. Jones[5], A. Kavanagh[9], M. King[11], D. Knight[11], R. Laman[11], T. Lankford[11], R. Lien[13], P. Lotz[11], M. Maimone[5], G. Marsh[11], R. Marshall[11], S. Martin[1], T. McFaden[11], R. Michell[1], D. Mitchell[7], M. Moffett[11], N. Morris[11], A. Mueseler[11], C. Nelson[11], L. Nguyen[1], W. Ogundere[11], K. Osbakk[13], D. Page[11], N. Paschalidis[1], R. Pfaff[1], C. Pirner[1], E. Pittman[11], J. Polidan[11], D. Puopolo[5], D. Raley[11], Z. Rawlings[1], P. Ribbens[4], E. Robertson[1], S. Rodriguez[11], G. Rosanova[11], B. Rose[11], T. Rosnack[1], T. Russell[11], M. Samara[1], B. Serabian[11], T. Sherman[11], R. Simonsen[13], T. Snyder[11], J. Søreng[13], V. Sutton[11], J. Sveen[13], D. Swanson[5], R. Swift[11], W. Taylor[11], R. Terwiliger[11], S. Tiede[11], C. Tucker[1], P. Uribe[1], H. Valentine[4], M. Wallace[1], F. Waters[11], L. West[11], B. West[11], T. Wilson[11], N. Wroblewski[11], S. Xu[7], D. Zarro[1] & E. Zesta[1]

[12]University Center in Svalbard, Longyearbyen, Svalbard and Jan Mayen. [13]Andøya Space, Andenes, Norway. [14]EISCAT Scientific Association, Kiruna, Sweden.

Article

Methods

Endurance instrumentation used in this study

We shall now give a brief description of the three scientific instruments carried by the rocketship from which data are directly used in this study. For more detailed information, see ref. 19.

Photoelectron spectrometer. The primary instrument aboard the *Endurance* was the PES consisting of eight boom-mounted dual electrostatic analyser (DESA) sensors (Extended Data Fig. 1), synchronized by a central main electronics box. The apertures of the eight sensors were physically aligned to view within 5° of the ambient magnetic field (look directions in and out of the page in Extended Data Fig. 1). Each sensor had two simultaneous look directions (field-aligned and anti-aligned) with a fixed 11° azimuth by 5° elevation field of view. The combined geometric factor of the eight DESA sensors was 1.8×10^{-3} $(cm^2\,sr\,eV\,eV^{-1})^{-1}$ for the aft-looking (A) sides, and 1.71×10^{-3} $(cm^2\,sr\,eV\,eV^{-1})^{-1}$ for the bow-looking (B) sides. The PES was sensitive to a differential energy flux down to 10^4 $(eV(cm^2\,sr\,eV)^{-1})$. The PES made 78 complete scans during the flight, each taking 10 s. Each scan produced two data products: a standard-resolution (15% $\Delta E/E$) measurement between 8.4 eV and 991.6 eV in logarithmic steps (Fig. 2b); and a high-resolution (0.5% $\Delta E/E$) scan between 20.30 eV and 25.85 eV in 0.15 eV steps (Fig. 2c).

For more information on the operational principle of the optics of the DESA sensor, see ref. 31. For a cross-section of the DESA sensor and a description of its test flight, see ref. 21.

Swept Langmuir Probe. SLP operates in plasma densities between 1×10^3 cm^{-3} and 1×10^9 cm^{-3}. SLP was a traditional Langmuir probe consisting of a gold-plated needle probe mounted at the tip of the Fo'c'sle of *Endurance* (Extended Data Fig. 1). Once every 5 s, a sweeping bias voltage (±5 V) was applied to the needle probe, and the resulting collected current was measured. Before flight, measured current (I) versus applied voltage (V_{SLP}) of SLP was calibrated in a thermal vacuum chamber from −30 °C to +50 °C. This resulted in less than 1% error in the in-flight measurement of I versus V_{SLP}. As is standard practice for a Langmuir probe, the total plasma density (n_e), electron temperature (t_e) and absolute spacecraft potential (ϕ_{SC}) are derived from fitting to the I–V curves measured during flight. For a time series of SLP measurements of n_e, t_e and ϕ_{SC}, showing 1σ errors, see Extended Data Fig. 4. The close agreement between independent measurements of n_e and t_e by SLP and EISCAT (Extended Data Fig. 6) and independent measurement of ϕ_{SC} by SLP and FIELDS (Fig. 3) give good confidence in SLP calibration and data analysis.

Electromagnetic Fields and Waves package. FIELDS (Extended Data Fig. 1) consisted of a pair of orthogonal 3.2-m (tip-to-tip) double probes in the plane perpendicular to the rocket axis (and therefore the magnetic field of Earth). Four spherical sensors with embedded pre-amps captured electrostatic and electromagnetic modes at frequencies between 5 Hz and 5 MHz.

Correction of electron measurements for spacecraft potential

Photoelectrons reaching the PES instrument fell through an additional potential drop arising from the electrical charging of the spacecraft (ϕ_{SC}). All exposed surfaces of the spacecraft were checked for electrical continuity before launch to ensure the chassis would provide a common electrical ground to all instruments and thus evenly distribute ϕ_{SC}. All measurements presented in this paper have been corrected for ϕ_{SC}, which was one of three plasma parameters measured directly by the SLP instrument (as described above; Extended Data Fig. 4). These spectra were then corrected for this potential using Liouville's theorem (converting through phase space density). For a full description of this technique, see, for example, Supporting Information S1 of ref. 13.

An additional independent cross-check of ϕ_{SC} was supplied by the mean potential of each FIELDS sensor (Fig. 3). FIELDS mean sphere

potentials floated during the flight according to ϕ_{SC} (Extended Data Fig. 5). These data were split before and after apogee, giving a relative change in potential ($\Delta\phi_{SC}$) on upleg and downleg. The absolute spacecraft potential could be directly measured by PES for periods when *Endurance* was in the photoelectron production layer (250–300 km) by comparing the measured energy of the $N_2\,A^2\Pi_u$ photopeak to its known energy of generation (24.09 eV). Using this calibration point, an estimate of absolute ϕ_{SC} was estimated for the upleg and downleg. This supporting measurement (Fig. 3a,b, grey dots) agreed within the errors to the primary measurement from SLP (Fig. 3a,b, black dots), giving good confidence in our determination of absolute ϕ_{SC}.

Method of calculation of potential drop from He-II photopeak measurements

Extended Data Fig. 2 shows two examples of PES scans illustrating the method for measuring the potential below the *Endurance*. Extended Data Fig. 2a,b shows PES scan 72, taken in the photoproduction region. Extended Data Fig. 2c,d shows PES scan 38, taken just after apogee in the exosphere. Extended Data Fig. 2b,d shows the high-resolution scans around the He-II photopeaks that resolved the peak dominated by $N_2\,A^2\Pi_u$ photoemission. For each scan, the energy of this peak was measured by fitting a six-term Gaussian (Extended Data Fig. 2b,d, blue line).

Extended Data Fig. 3a,d shows the peak energy of the $N_2\,A^2\Pi_u$ photopeak as measured throughout the flight by PES (Extended Data Fig. 3a, upleg, and Extended Data Fig. 3d, downleg). Measurements during ACS firings have been removed as this substantially perturbed the spacecraft potential and ambient plasma environment.

Horizontal error bars come from four sources: (1) the inherent 0.5% $\Delta E/E$ energy resolution of the sensor; (2) the estimated error in the measurement of spacecraft potential from SLP (and FIELDS for the supporting cross-check measurement); (3) the errors in the peak fitting resulting largely from Poisson noise in the data. This error source was most prevalent above 700 km as the $N_2\,A^2\Pi_u$-dominated main photopeak became increasingly degraded through Coulomb collisions on their journey up from the photoproduction region (Fig. 3d); and (4) the error arising from the weak electrical current induced within the structure of the conductive spacecraft from its motion through the magnetic field of Earth ($\mathbf{E}_{motional} = -\mathbf{V}_{Endurance} \times \mathbf{B}$). These induced currents will result in a very small potential difference between the common electrical ground of the PES sensors, and hence an error in their measurement of the energy of the photopeaks. However, when measurements of $\mathbf{V}_{Endurance}$ from the on-board GPS receiver were combined with the on-board magnetometer[19], this final error was found to be very small (<0.05 V in a 0.55 V potential drop), but it is nonetheless included in our error analysis.

Extended Data Fig. 3b,e shows the peak energy of the $N_2\,A^2\Pi_u$-dominated main photopeak after correction for the time-varying spacecraft potential (ϕ_{SC}) by SLP (Extended Data Fig. 3b, upleg, and Extended Data Fig. 3e, downleg). After correction, measurements of the $N_2\,A^2\Pi_u$ photopeak in the photoproduction region (250–300 km) were within the errors of its known atomic value of 24.09 eV, giving strong confidence in the accuracy of our measurement of ϕ_{SC} throughout the flight. To calculate the potential drop below the spacecraft, this corrected photopeak energy is subtracted from its known production energy of 24.09 eV. The result is shown in Extended Data Fig. 3c (upleg) and Extended Data Fig. 3f (downleg) and also in Fig. 3a,b.

The total potential drop on the upleg was 0.56 ± 0.09 V, corresponding to a 1.10 µV m^{-1} electric field parallel to the magnetic field. The total potential drop on the downleg was 0.54 ± 0.09 V, corresponding to a 1.07 µV m^{-1} parallel electric field.

Theory of the generation of ionospheric ambipolar electric fields

In this section, we derive the ambipolar electric field from the first principles, including why it is generally assumed to be dominated by

the electron pressure gradient (∇P_e). The existence of such planetary-scale electric energy fields has long been predicted by theoretical studies[11,24,25]. Although these studies approach the problem slightly differently, all involve solving the time-varying plasma momentum equation (equation (1)) for parallel electric field ($E_\parallel$). All arrive with the same fundamental prediction that the outward pressure on the topside ionospheric of Earth should generate a global-scale parallel electric field.

$$\underbrace{\frac{\partial}{\partial t}(A\rho_e u_e)}_{1} + \underbrace{\frac{\partial}{\partial r}(A\rho_e u_e^2)}_{2} + \underbrace{A\frac{\partial P_\parallel}{\partial r} - A\frac{(P_\parallel - P_\perp)}{B}\frac{\partial B}{\partial r}}_{3}$$
$$= An_e(\underbrace{-qE_\parallel}_{4} \underbrace{- m_e g}_{5}) + \underbrace{A\frac{\delta m_e}{\delta t}}_{6} + \underbrace{Au_e S_e m_{rme}}_{7} \tag{1}$$

Equation (1) describes the generalized balance of electron momentum ($\rho_e = m_e q$) in a magnetic flux tube of area A, which expands with distance r from the centre of Earth (and u_e is bulk electron velocity). Term 1 describes momentum density, which is the momentum inherent at a given distance from Earth (r) along the flux tube. Term 2 is the net flux of momentum being transported into this region of the flux tube. Note that in this derivation we are working in the observer frame (sometimes called the laboratory frame), and thus terms 1 and 2 must be separated. (When equation (1) is solved in the frame of a fluid parcel, terms 1 and 2 can be combined into a single term called the convective derivative). The final term on the left-hand side (term 3) is the gradient of electron pressure, which provides a net force and hence an impulse to the electrons, changing their momentum. Equation (3) separates the contributions from electron pressure parallel ($P_\parallel$) and perpendicular ($P_\perp$) to the magnetic field.

The right-hand side of equation (1) describes the four fundamental sources of electron momentum at a given distance from Earth (r). The first and foremost is the net force on the electrons with charge $-q$ from the electric field $E_\parallel$ (term 4). Next is the downward force of gravity ($m_e g$ and term 5). Term 6 is the collisional term, broadly describing any momentum exchange arising from collisions of electrons with ions or neutral atoms (for example, Coulomb collisions and inelastic scattering). Term 7 is the production term, describing the increase in electron momentum arising from the creation of new electrons (at a rate S_e particles per second) at a given distance along the flux tube (r).

Before we solve equation (1), we will make three common assumptions when describing ionospheric electrons. First, as electrons move very quickly and respond almost instantaneously to changes in the system, we will assume that the bulk population of ionospheric electrons is in a steady state ($\partial/\partial t = 0$). This is consistent with the EISCAT radar observations of the ionosphere throughout the *Endurance* mission, the structure of which was stable and constant during the flight (for example, consistent with this steady-state assumption). Thus, we may ignore term 1 of equation (1).

For our next assumption, we will consider that the electron mass is so small that to the first order we can ignore any term containing m_e (refs. 6,11,24,25). For more thorough derivations of $E_\parallel$ in which the terms including m_e are carried all the way through, see refs. 11,24,25. However, here for brevity, we will simplify the electron momentum equation as follows:

$$A\frac{\partial P_\parallel}{\partial r} - A\frac{(P_\parallel - P_\perp)}{B}\frac{\partial B}{\partial r} = -An_e qE_\parallel \tag{2}$$

Finally, as per most ionospheric models, we will assume that the bulk population of ionospheric electrons are isotropic ($P_\parallel = P_\perp = P_E$). In reality, satellite measurements at the altitudes and latitudes explored by *Endurance* have shown a small degree of anisotropy in ionospheric electrons; however, this is of the order of only about 10–20% (ref. 32), and thus to the first order the assumption of isotropy is quite reasonable.

Note that although the second term of equation (2) has a negative sign in front of it, the magnetic field (B) gets weaker with distance (r) (that is, $\partial B/\partial r$ points downwards), and thus overall this term is a net positive to the momentum equation. Assuming electron isotropy removes this additional term, and thus results in a more conservative approximation of $E_\parallel$. With all these approximations made, we thus arrive at the final form of the steady-state momentum equation for ionospheric electrons:

$$A\frac{\partial P_E}{\partial r} = -An_e qE_\parallel \tag{3}$$

We may now re-arrange and solve for the predicted parallel electric field:

$$E_\parallel = \frac{1}{n_e q}\frac{\partial P_E}{\partial r} = -\frac{\nabla P_E}{n_e q} \tag{4}$$

To test this prediction, we measured the gradient of electron pressure throughout the flight by the SLP instrument (Extended Data Fig. 4). Taking the gradient and then integrating with distance along the field line ($\int -\nabla P_E/n_e q\, dr$) gives a prediction of the total accumulated vertical potential drop from equation (4). For the first time, we are thus able to compare directly with observations (Fig. 3a,b), finding a close agreement between this theory and observations (as described in the main text of this paper).

Ambipolar diffusion theory and calculation of altitude plasma density profiles

According to ambipolar diffusion theory, we consider the ionosphere as an isothermal hydrostatic ion atmosphere with a simple density profile given by

$$n(s) = n_0 \exp\left(-\frac{s - s_0}{H}\right) \tag{5}$$

where n is the density of plasma at altitude s above a reference altitude s_0. H is defined as the scale height of the ionosphere and is given by

$$H = \frac{k_b T_i}{(m_i g) - (q E_\parallel)} \tag{6}$$

where k_b is the Boltzmann's constant, T_i is the ion temperature, m_i is the ion mass, g is the gravitational acceleration and q is the ion charge. Simply put, this theory implies that the electric field ($E_\parallel$) effectively counters gravity, increasing the scale height of the ionosphere. As H shows up in the exponent of equation (5), this theory predicts that the presence of $E_\parallel$ has an amplified effect on the plasma density at high altitudes.

Endurance measurements of $n(s)$, T_i and, for the first time, $E_\parallel$ can be combined with equations (5) and (6) to provide an additional cross-check on the interpretation of the photoelectron peak shift as resulting from an ambipolar electric field. We take the base density ($n_0 = 1.9 \times 10^{11}$ cm^{-3}) as measured by SLP at the top of the F-region of the ionosphere ($s_0 = 300$ km). EISCAT radar measured a quasi-isothermal ion temperature profile during the flight with mean temperature (T_i) of 1,453 ± 376 K on the upleg and 1,614 ± 648 K on the downleg. We assume a mean ion atomic mass (m_i) of 15.9 dalton as per the International Reference Ionosphere empirical model. These equations are used to calculate the altitude versus density profiles in Fig. 1.

Data availability

Endurance ephemeris data and all science data presented in this article are available at the Space Physics Data Facility of NASA (https://spdf.gsfc.nasa.gov/data_orbits.html) through the Coordinated Data

Article

Analysis Web (CDAWeb) tool (https://cdaweb.gsfc.nasa.gov/) by selecting 'Sounding Rockets' from the data sources.

31. Collinson, G., Chornay, D. J., Glocer, A., Paschalidis, N. & Zesta, E. A hybrid electrostatic retarding potential analyzer for the measurement of plasmas at extremely high energy resolution. *Rev. Sci. Instrum.* **89**, 113306 (2018).
32. Oyama, K. & Takumi, A. Anisotropy of electron temperature in the ionosphere. *Geophys. Res. Lett.* **14**, 1195–1198 (1987).

Author contributions The *Endurance* mission and its overall methodology were conceived by G.A.C. and A. Glocer, who acquired the funding, administered the science team and drafted this paper. The instruments were developed by G.A.C., R.P., A. Barjatya, R. Clayton, A. Breneman, J.C., R.M., L.D., E.R., D.S., L.N., P.U., T.C., A. Ghalib, H.V., N.G. and S.D. Data analysis was performed by G.A.C., A. Glocer, R.P., A. Barjatya, R. Conway, A. Breneman, J.C., F.E., D.M., S.I., H.A., L.D., A.K., D.S., S.X. and J.M.
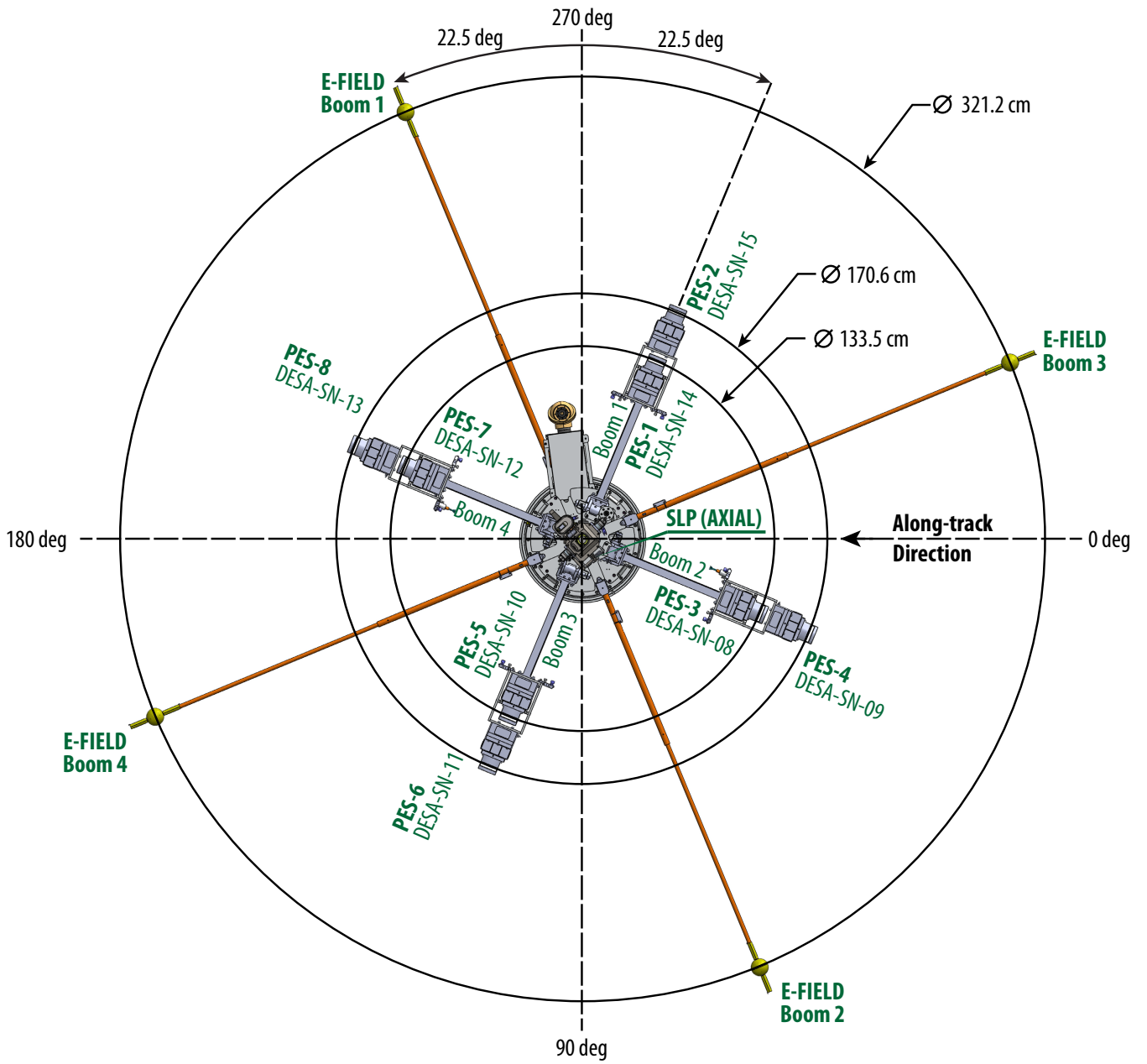
Extended Data Fig. 1 | Layout of the *Endurance* spacecraft showing scientific instruments used in this study. View from above looking aft. Magnetic field into page on upleg and out of page on downleg.

Article
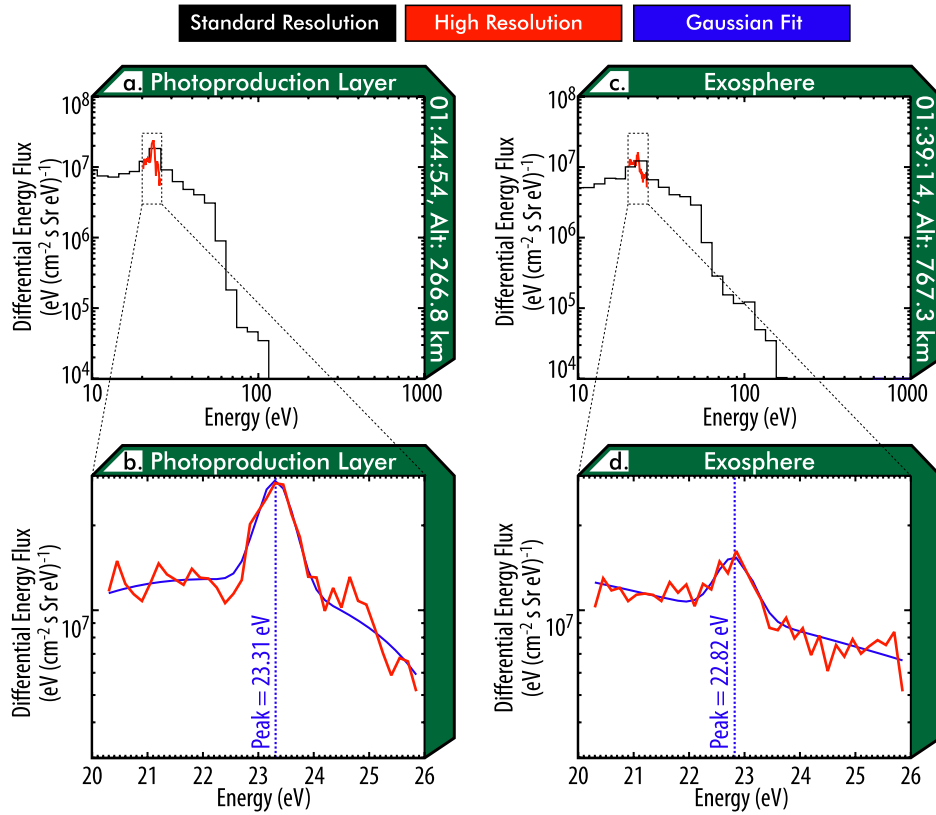
Extended Data Fig. 2 | Example spectra from the Photoelectron Spectrometer. Data calibrated but uncorrected for spacecraft potential. **a**, PES Scan 72 showing standard resolution (black) and high resolution (red). **b**, PES Scan 72 zoomed in to the He-II photopeaks showing a gaussian fit (blue) to the primary $N_2\,A^2\Pi_u$ dominated photopeak. **c**,**d**, The same for PES Scan 38.
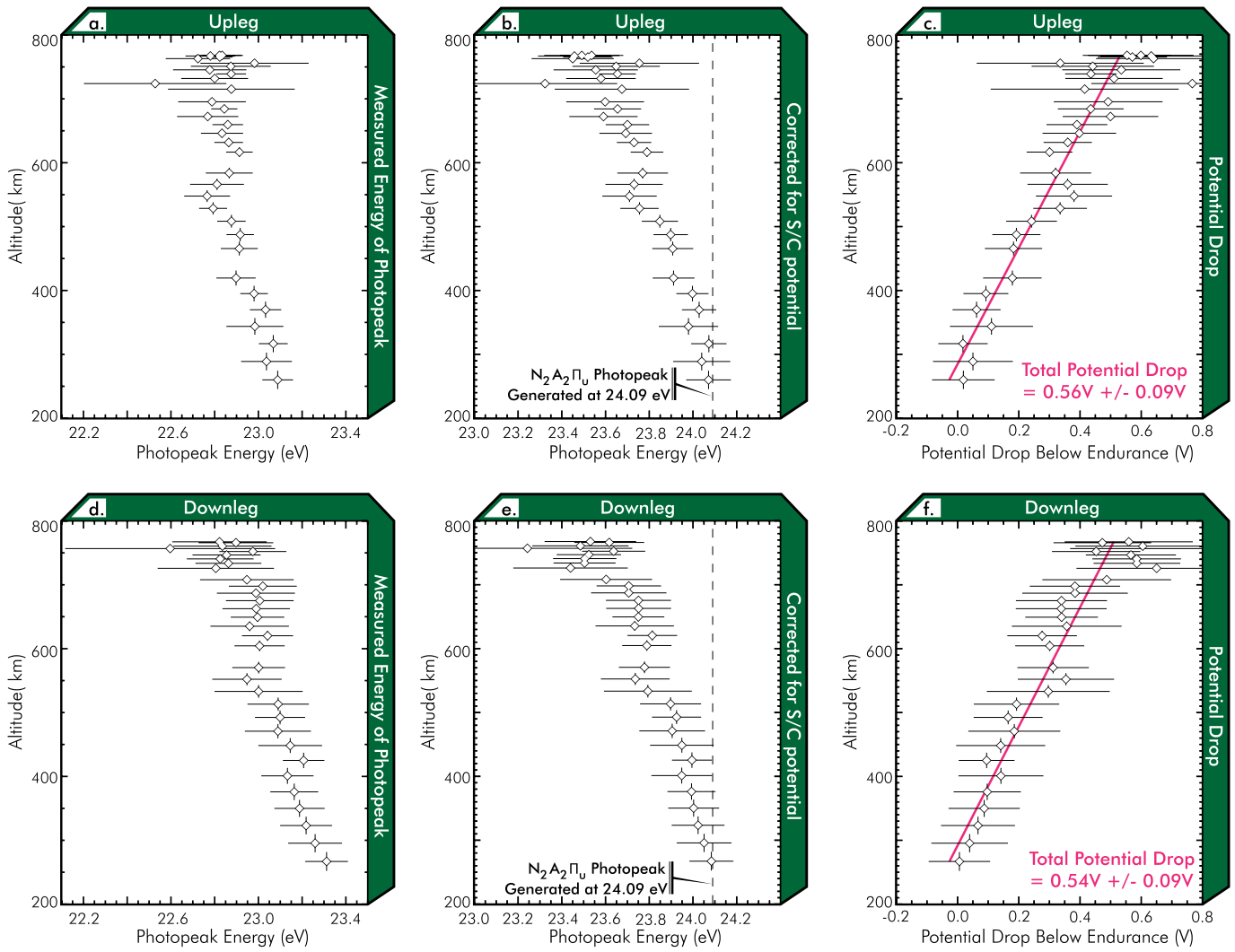
Extended Data Fig. 3 | Conversion from peak energy of photopeaks to planetary potential drop below *Endurance*. Upleg, top panels; downleg, bottom panels. **a**,**d**, Peak energy of $N_2 A^2\Pi_u$ dominated photopeak as measured. **b**,**e**, Energy of photopeak after correction for S/C potential from SLP. **c**,**f**, Potential drop below *Endurance* (as Fig. 2a,b).

Article
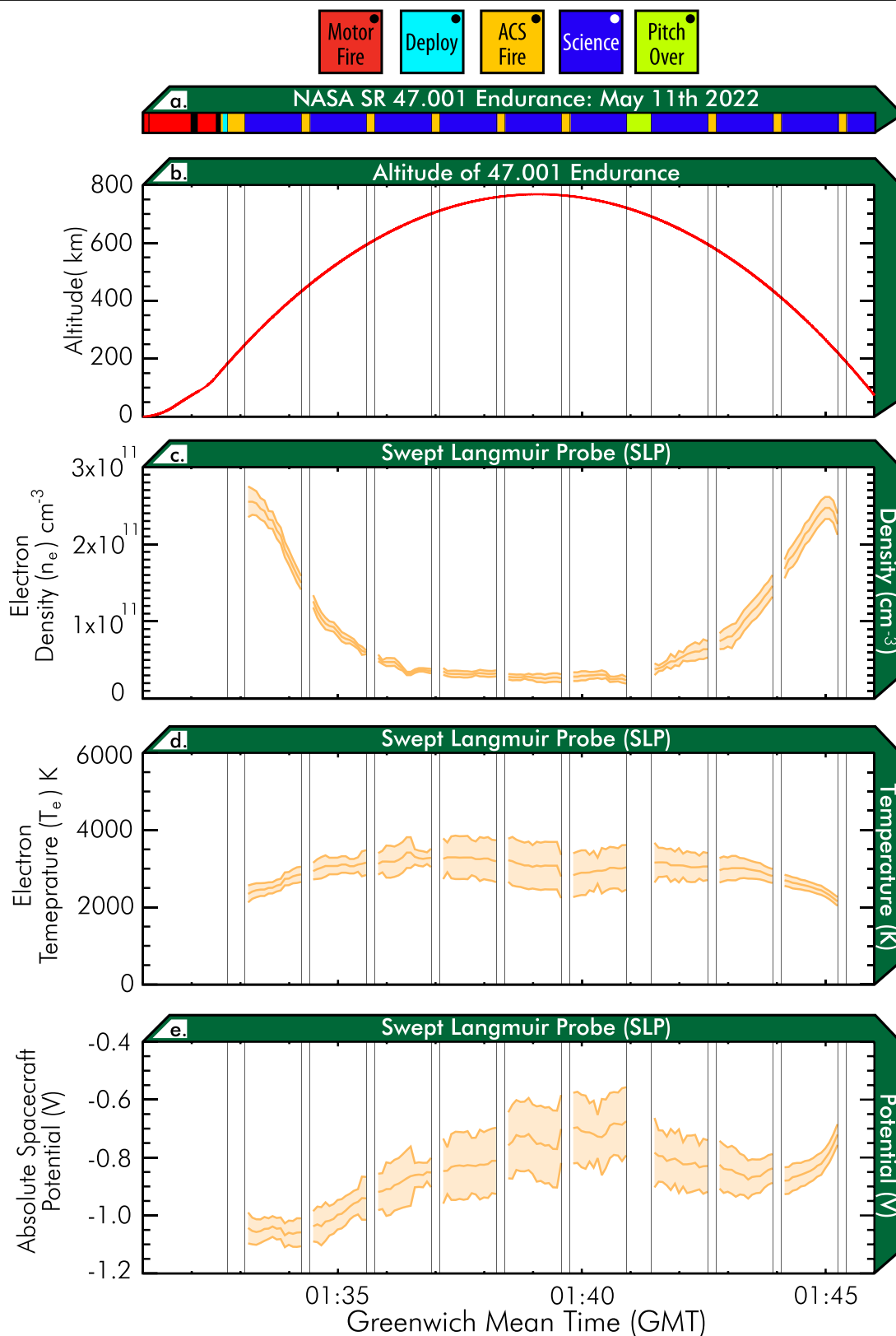
Extended Data Fig. 4 | Measurements by the Swept Langmuir Probe. Area denotes ±1σ error. **a**, Colour-coded timeline of *Endurance* mission (as per Fig. 1a, Fig. 2a). **b**, Altitude versus time. **c**, Total Electron density (cm⁻³). **d**, Electron temperature (K). **e**, Potential difference between *Endurance* and ambient plasma.

The periodic (70 s) firing of the ACS thrusters (amber, panel **a**) temporarily perturbed the plasma environment around the spacecraft. The resulting erroneous measurements by SLP have been cut from the dataset.
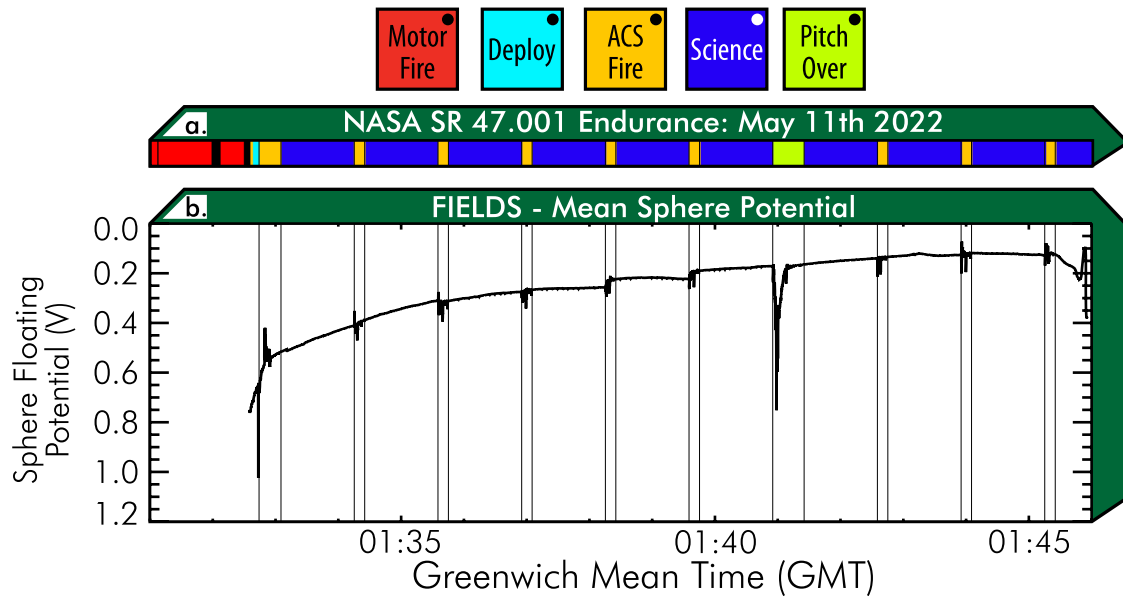
Extended Data Fig. 5 | Supporting Measurements by the FIELDS instrument. a, Colour-coded timeline of *Endurance* mission (as per Fig. 1a, Fig. 2b). **b**, Mean potential between the two pairs of electric field probes.
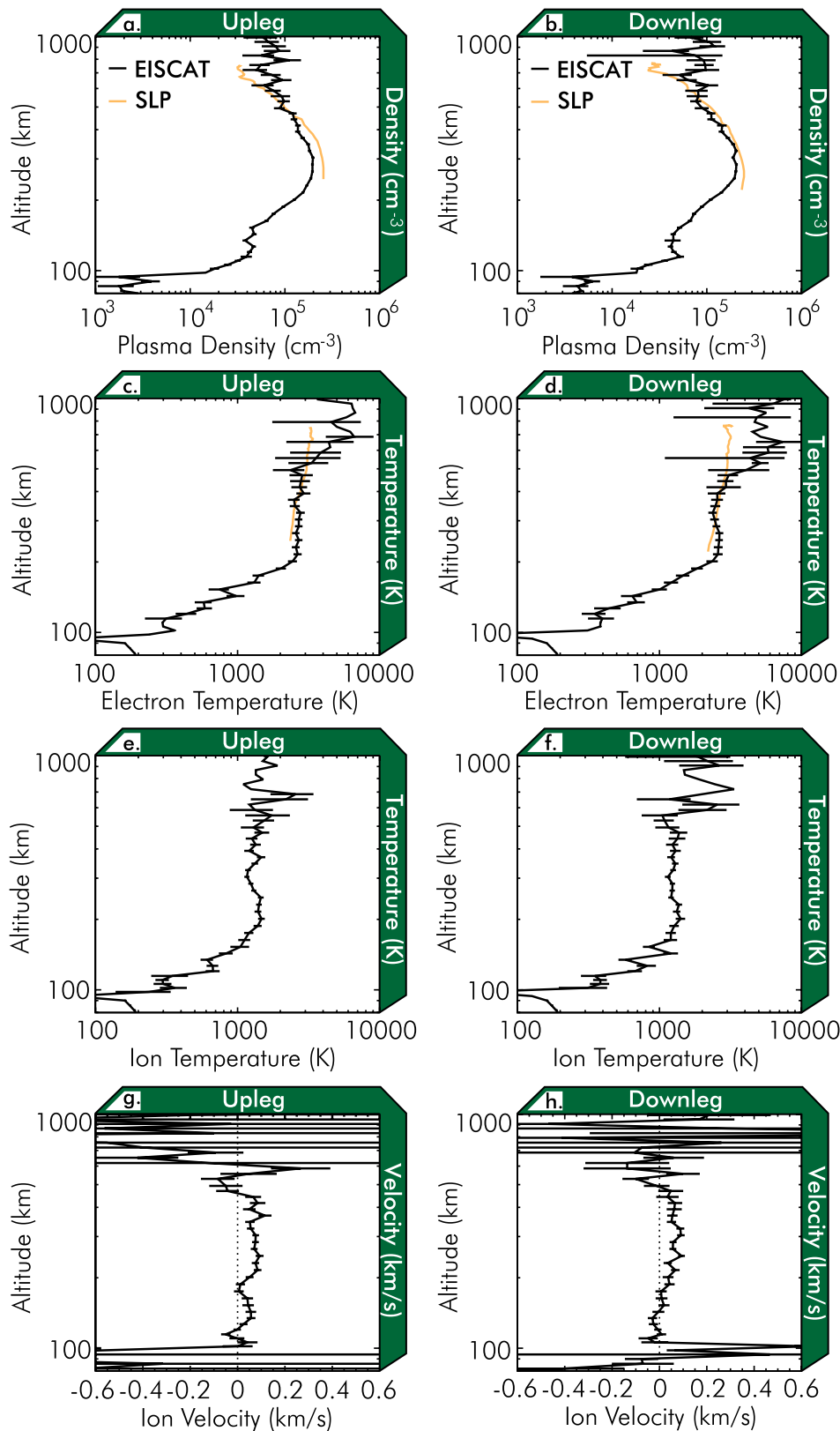
Extended Data Fig. 6 | Radar measurements from the EISCAT Radar in black compared to in situ measurements by the SLP instrument in gold. a,b, Plasma density; **c,d,** Electron temperature. **e,f,** Ion temperature; **g,h,** Ion velocity. These plots were made by time-averaging measurements from the upleg and downleg portion of the flight. Error bars represent the standard deviation.

EISCAT data were truncated above 500 km in Fig. 3 owing to the large error bars but are shown here in full. The good agreement between independent measurements of n_e and t_e by EISCAT and SLP give good confidence in our SLP data analysis.
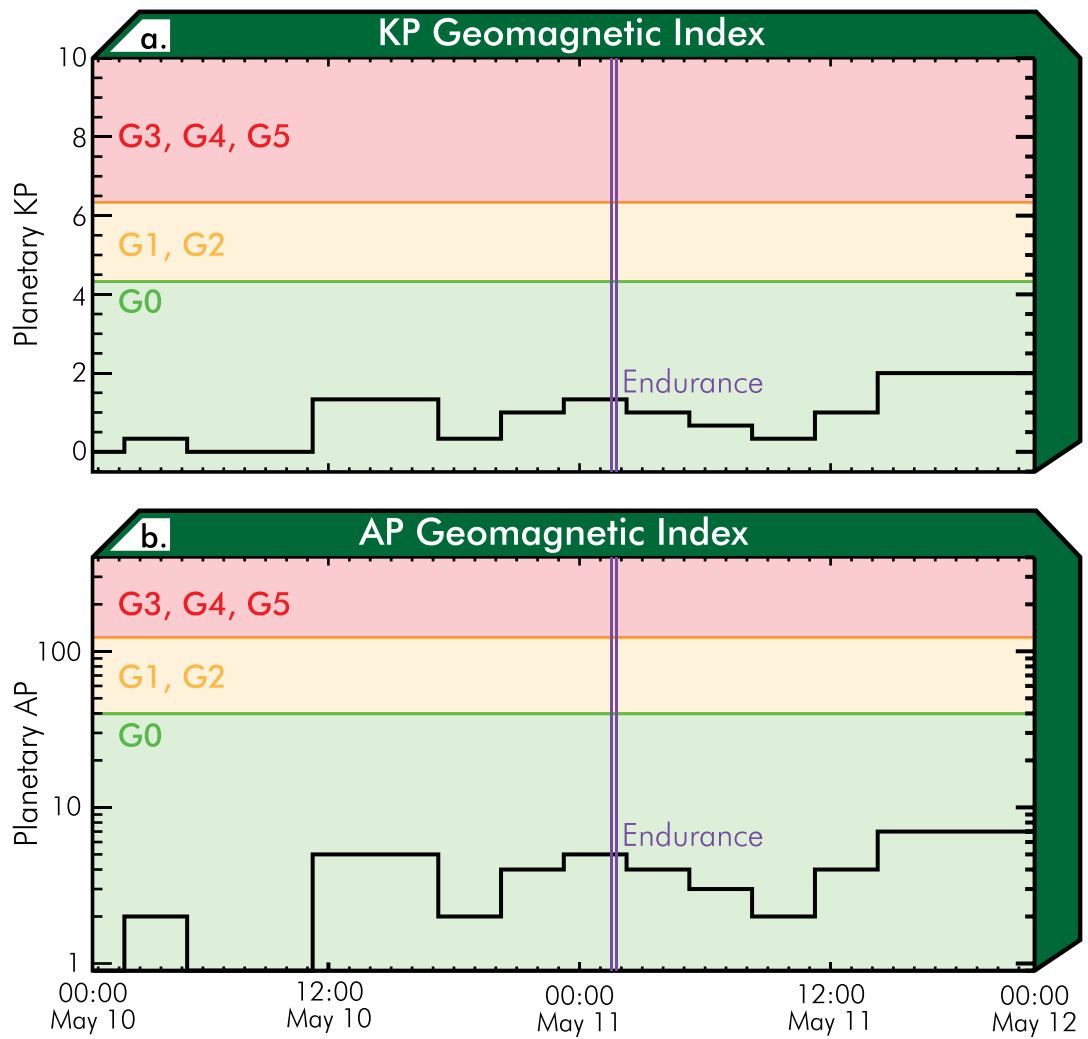
Extended Data Fig. 7 | Geomagnetic activity for the two days surrounding the launch of *Endurance*. a, Planetary KP index; **b**, planetary AP index. Both indexes show low activity (G0).